Scaffold-Oriented Asymmetric Catalysis: Conformational Modulation of Transition State Multivalency during a Catalyst-Controlled Assembly of a Pharmaceutically Relevant Atropisomer

Nicolò Tampellini, Brandon Q. Mercado, Scott J. Miller*

Department of Chemistry, Yale University, New Haven, Connecticut 06520, United States

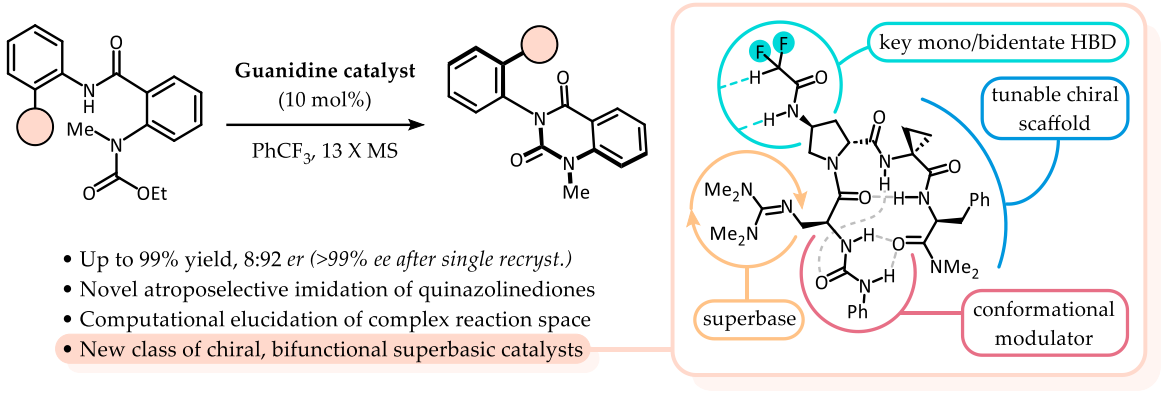

ABSTRACT: A new class of superbasic, bifunctional peptidyl guanidine catalysts is presented, which enable the organocatalytic, atroposelective synthesis of axially chiral quinazolinediones. Computational modeling unveiled the conformational modulation of the catalyst by a novel phenyl urea N-cap, that shape-shifts the structure into the active, folded state. A previously unanticipated noncovalent interaction involving a difluoroacetamide acting as a hybrid mono- or bidentate hydrogen bond donor emerged as a decisive control element inducing atroposelectivity. These discoveries spurred from a scaffold-oriented project inspired from a fascinating investigational BTK inhibitor featuring two stable chiral axes, and relies on a mechanistic framework that was foreign to the extant lexicon of asymmetric catalysis.

Introduction. Chemical transformations with limited or no enantioselective precedent present the ideal case study for the development of new asymmetric catalytic methods, particularly when current catalysts are unable to deliver an efficient and selective transformation. In this context, we were inspired by an investigational BTK inhibitor developed by Bristol-Myers Squibb (BMS-986142) possessing two stable axes of chirality and developed as a single diastereomer[1]. Noteworthy in this context is the importance of the *N*-aryl quinazolinedione motif in drug discovery, as also demonstrated by the recently approved drug carotegrast methyl[2] as well as in elinogrel[3] (development terminated in 2012). Despite the considerable momentum in the area of atroposelective catalysis,[4] studies of enantioselective *N*-aryl quinazolinedione formation are scant, featuring a singular report from a process group at BMS itself describing a Ni(0)-catalyzed isocyanate insertion[5]. Furthermore, we were able to find no report of an organocatalytic atroposelective quinazolinedione-forming reaction, which prompted us to pursue a scaffold-targeted catalyst discovery project in an area of chemical space of current pharmacological interest.

Following the process route for BMS-986142[1b], we set out to adapt the mechanistic paradigm for the critical cyclization step shown in **Figure 1** to furnish axially chiral quinazolinediones. We envisioned the use of a chiral superbase such as a guanidine could catalyze the multistep cyclization in an enantioselective fashion. Mindful of recent advancements in asymmetric superbase catalysis,[6] we sought to expand recent work from our group that described the incorporation of a tetramethylguanidine group on peptidyl frameworks.[7] These backbones proven adaptable to many types of chemical transformations,[8] with ubiquitous operation on selectivity-defining noncovalent interactions.[9]

In this context, we perceived that the development of a new catalyst would be as valuable as the detailed understanding of its workings, particularly for an unprecedented transformation. Therefore, we brought to focus the mechanistic complexity of the catalyst and the transformation through a detailed, large-scale

computational modeling of the reaction. As many other modern, enabling chiral catalysts, the incorporation of flexible elements and polar functionality stand out as noncanonical with respect to classical, sterically driven chiral catalysts.[6d, 8b, 8c, 10] However, the experimental and computational exploration of this dynamic and multifunctional catalyst space can prove demanding, particularly for reactions lacking detailed mechanistic understanding. The increased number of tunable variables on the catalyst increases the likelihood of interdependent effects, concealing the direct observation and leverage of clear, elementary trends. In view of this, *ab initio* methods offer an orthogonal, quantum mechanics-based perspective to the dissection of complex relationships manifesting experimentally through monodimensional, often cryptic readouts (yield, enantiomeric excess, reaction rate). This approach becomes increasingly relevant for more complex systems, where chemical intuition and basic soft models fail in predicting reaction outcomes and in describing the role of individual elements present on the catalyst and on the substrate.

Presented below is a successful experimental and computational campaign that delivered a new and selective catalyst for this unprecedented atroposelective cyclization. In addition, the study reveals striking insights about the reaction coordinate, which include a conformational activation of the catalyst, specific activation modes for each stereoisomer, and the unique ability of a difluoroacetamide group to induce atroposelectivity. To the best of our knowledge, we found no reports in the literature of a chiral catalyst leveraging this group and this peculiar non-covalent interaction.

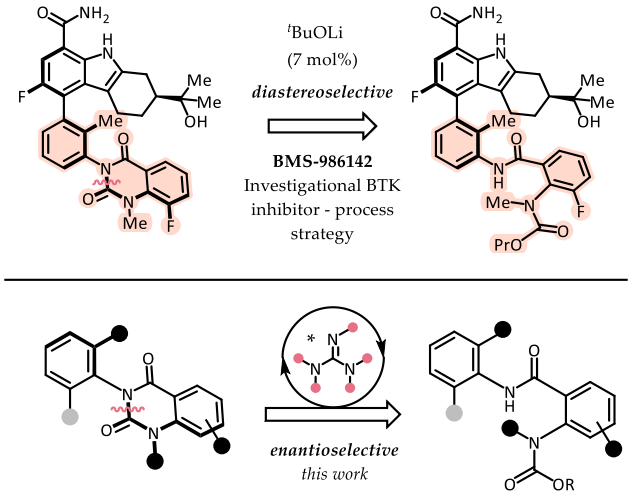

Figure 1. Atroposelective imidation strategy to access axially chiral quinazolinediones.

Results and Discussion. Our investigation began with the synthesis of methyl carbamate **1a** as a model system for BMS-986142 (**Figure 1** and **2**). When subjected to catalytic quantities of superbases, partial conversion to quinazolinedione **2a** was observed. Exploration of known chiral superbases was not fruitful. While Bandar-Lambert's cyclopropenimine[11] **3** showed some activity (21% conv., **Figure 2**, entry a), a racemic product was obtained. The less basic Núñez-Dixon's iminophosphorane[12] **4** was almost inactive exhibiting only 3% conversion to the product (entry b), although hints of atroposelectivity could be detected (38:62 er). Interestingly, chiral peptidyl guanidines, although of comparable basicity to **4**, showed a range of activities, even outperforming **3** (0-35% conv., **Figure 2**, entries c-e). Since conversion did not show a clear dependence on the basicity of the catalyst (see **Figure 2** pK_a(BH$^+$) values), we reasoned that differently tailored multifunctionality of peptidyl guanidines had to be responsible for the increased activity we were observing for some of these catalysts (entries c-e). The introduction of various single-point changes to these structures eventually resulted in the discovery of catalyst **P1**, which exhibited remarkable activity and the highest level of enantioselectivity we had seen so far (100% conv., 25:75 er, entry f). Strikingly, the combination of a *N'*-phenyl carbamoyl *N*-terminus end cap and a difluoroacetamide substituent branching off the proline backbone had a synergistic effect in catalyzing the reaction, while similar catalysts with just one of these two features were both significantly less active and less selective (entries d-f).

Further fine-tuning of the catalyst following a traditional single-point modification tenet afforded equally active and more selective catalyst **P4** (100% conv., 17:83 er, entry i). Nonetheless, we observed non-additive effects with certain pairs of point modifications that challenge this classical optimization protocol. As an example, the i+2/*C*-terminus pair Acpc/NMe$_2$ performed better than the Aib/NHMe pair, even though the individual point changes alone afforded less selective catalysts (entries f-i). The electronic and the steric profiles of the pendant amide at the 4' position of the proline ring were also tuned, and the best performing group was identified as the difluoroacetamide of catalyst **P4**. Notably, the unique performance of the difluoroacetamide-containing catalyst **P4** among its congeners was unexpected and enigmatic. Point modifications at this position yielded dramatic effects: whereas the difluoroacetyl catalyst led to 100% conversion to the product and 83:17 er (**Figure 2**, sub-table, **P4**), the corresponding trifluoroacetyl congener was completely inactive (<1% conversion; **Figure 2**, sub-table, **P8**). The acetyl congener saw some restored conversion at 35%, but selectivity remained minimal (58:42 er, **Figure 2,** sub-table, **P6**). Other substitutions are shown in **Figure 2** and contributed to further structure-selectivity considerations that we studied in greater depth and are presented in the following sections.

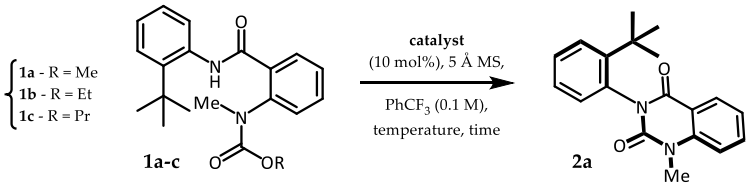

entry	catalyst	R	T (°C)	time (h)	% conv.[a]	er[b]
a	Lambert's cyclopropenimine **3**	Me	23	15	21	50:50
b	Dixon's iminophosphorane **4**	Et	23	15	3	38:62
c	Boc-TMGA-(αMe)^{D}Pro-Acpc-Phe-NMe_2	Me	23	15	34	55:45
d	**PhNHCO**-TMGA-(αMe)^{D}Pro-Acpc-Phe-NMe_2	Me	23	15	5	52:48
e	Boc-TMGA-(**4*S*-DFA**)^{D}Pro-Acpc-Phe-NMe_2 *(P0)*	Me	23	15	*traces*	-
f	**PhNHCO**-TMGA-(**4*S*-DFA**)^{D}Pro-Aib-Phe-NHMe *(P1)*	Me	23	15	100	25:75
g	PhNHCO-TMGA-(4*S*-DFA)^{D}Pro-Aib-Phe-**NMe_2** *(P2)*	Me	23	15	53	40:60
h	PhNHCO-TMGA-(4*S*-DFA)^{D}Pro-**Acpc**-Phe-NHMe *(P3)*	Me	23	15	27	43:56
i	PhNHCO-TMGA-(4*S*-DFA)^{D}Pro-**Acpc**-Phe-**NMe_2** *(P4)*	Me	23	15	100	17:83
j[c]	PhNHCO-TMGA-(4*S*-DFA)^{D}Pro-**Acpc**-Phe-**NMe_2** *(P4)*	Et	23	15	100	14:86
k[c,d]	PhNHCO-TMGA-(4*S*-DFA)^{D}Pro-Acpc-Phe-NMe_2 *(P4)*	**Pr**	23	15	77	16:84
l[c,d]	PhNHCO-TMGA-(4*S*-DFA)^{D}Pro-Acpc-Phe-NMe_2 *(P4)*	**Et**	-15	40	>99	8:92

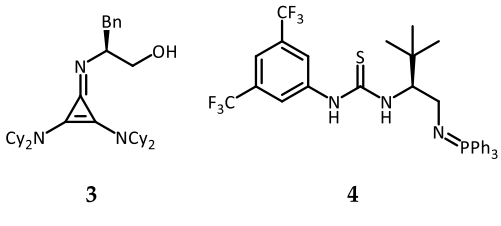

p*K*$_a$(BH$^+$, **3**, MeCN) ~ 26.9

p*K*$_a$(BH$^+$, $CyNPPh_3$, MeCN) ~ 22.7

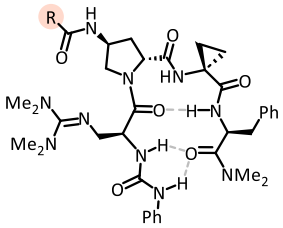

p*K*$_a$(BH$^+$, BTMG, MeCN) ~ 23.6

R	conv.	*ee*
CHF_2	100%	66% *ee* (**P4**)
PhNH	100%	15% *ee* (**P5**)
CH_3	35%	6% *ee* (**P6**)
CH_3O	10%	16% *ee* (**P7**)
CF_3	<1%	(**P8**)
Ph	<1%	(**P9**)

sub-table

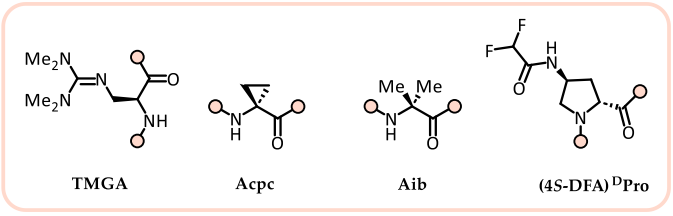

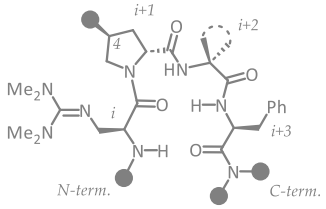

Figure 2. Optimization highlights. Reactions were run at a 0.025 mmol scale. **a**: Conversion estimated by chiral HPLC UV trace at 254 nm, uncorrected. **b**: Enantiomeric excess presented by order of elution on chiral HPLC column. **c**: Reaction performed at 0.2 M concentration. **d**: 13X MS used instead of 5 Å MS. **Sub-table**: reactions with **P4-P9** performed at 23 °C for 15 h. BTMG: 2-(tert-butyl)-1,1,3,3-tetramethylguanidine (Barton's base).

Substrate Exploration. At this stage, we also explored the effects of leaving group modifications on the benzamide substrate (**Figure 2**, **1a-c**). Homologating the methyl carbamate (**1a**, R=Me) to an ethyl carbamate (R=Et, **1b**) improved selectivity (100% conv., from 17:83 er to 14:86 er, entries i and j). Further homologation to the propyl carbamate (**1c**, R=Pr) reduced reaction conversion without improving selectivity (77% conv., 16:84 er, entry k). Pleasingly, ethyl carbamate **1b** proved reactive even at lower temperatures, and minor alterations to the reaction conditions were able to afford product **2a** in >99% conv. (99% isolated yield) and 8:92 er ($PhCF_3$ 0.2 M, 13X MS, -15 °C, 40 h, entry l). Notably, the product **2a** could be recrystallized to >99:1 er.

With a selective system in hand, a structure-activity relationship study was performed on analogs of substrate **5a** (**Figure 3**). Ethylated and brominated analogs **5b** and **5c** retained satisfactory selectivity (24:76 er and 26:74 er, respectively), but to our surprise, both substitutions heavily jeopardized reaction rate relative to **5a**. Relative conversion rates were estimated around two to three orders of magnitude slower (based on uncorrected HPLC

conversion). Similarly, thieno-fused substrate **5d** cyclized slowly, but with good enantioselectivity and yield (97%, 18:82 er). Enantioenriched crystals of products **2a** (>1:99 er), **2c** (6:94 er), and **2d** (>1:99 er) were used to determine the absolute configuration of the major enantiomer of each product, which was determined to be S_a in all three cases. This notion proved critical in validating our computational study, presented below. When the size of the *tert*-butyl substituent is reduced to a trifluoromethyl (**5e**), reaction rate is satisfactory, but selectivity decreases significantly compared to the parent compound **5a** (87%, 34:66 er). Interestingly, the introduction of a second *tert*-butyl group on the ring dramatically reduced both reaction rate and selectivity (**5f**, 43% ^{1}H NMR conv., 56:43 er). The different degrees of compatibility between the R^1 and R^2 substituents within **5** and the catalyst **P4** stimulated a deep inquiry into the physical reasons behind the dramatic effects underlying the high degree of specificity we had observed.

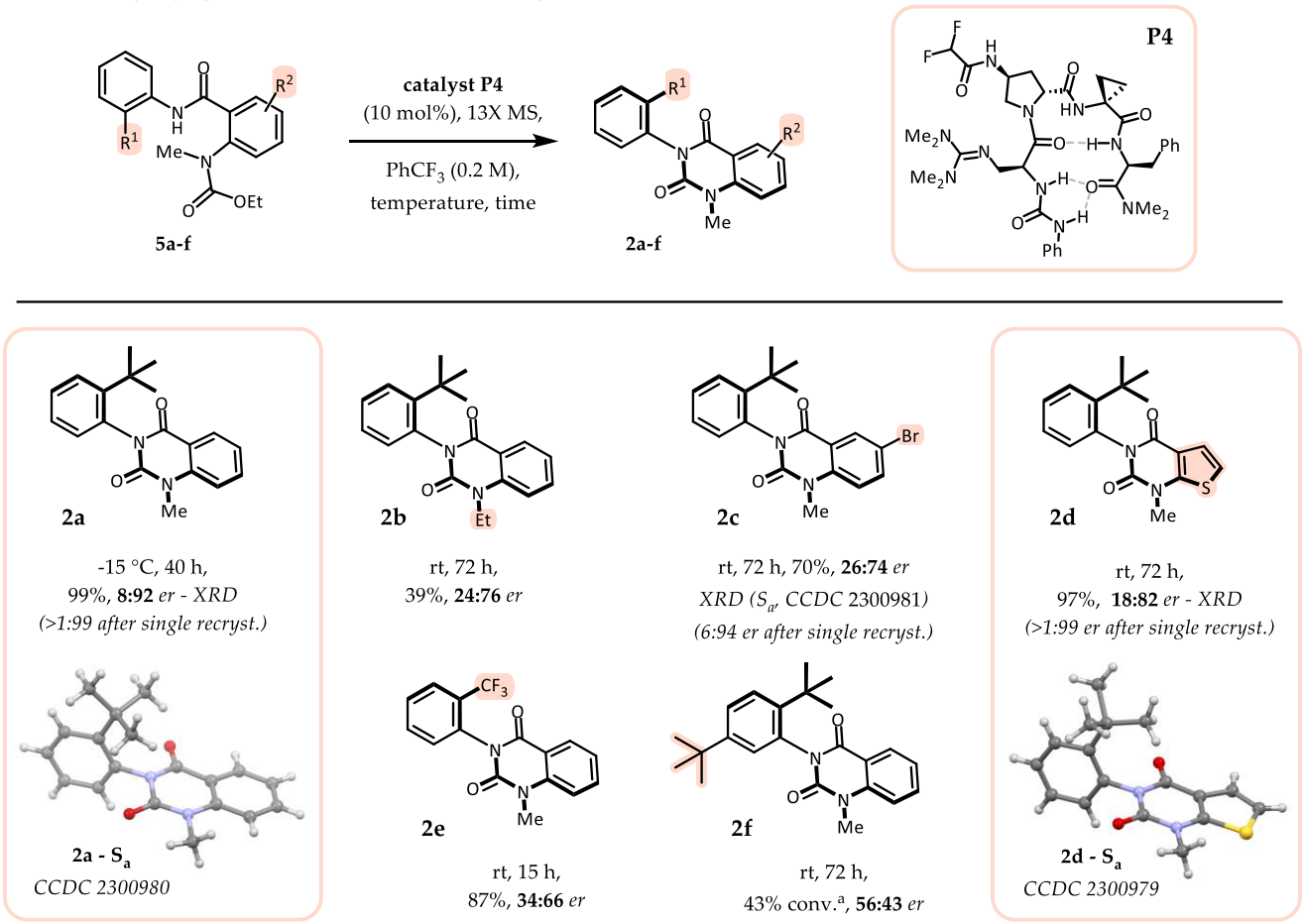

Figure 3. Substrate exploration and crystallographic determination of the absolute configuration. Reactions were run on a 0.05 mmol scale. **a**: conversion determined by ^{1}H NMR; **2f** not chromatographically separable from **5f**.

Computational Modeling. Intrigued by the origin of selectivity and specificity of the reaction, as well as the uniqueness of the lead catalyst compared to previous works from the group, we decided to conduct a computational modeling of this atroposelective imidation. Exhaustive *in silico* studies on flexible tetrameric peptide catalysts are very rare,[9c, 9g, 9i] presumably because of the challenge associated with their conformational complexity.[8a, 8b, 13] Nevertheless, we envisioned that leveraging modern, efficient computational tools would help in taming this complexity. Detailed computational methodologies can be found in the Supporting Information. Throughout, reported energetic data was computed at the M06-2X/def2-QZVP/CPCM($PhCF_3$)//R^{2}SCAN-3c/CPCM($PhCF_3$) level.

Internal H-bonding topology as an enabling feature for catalysis. The first striking observation of the experimental work that we wished to understand was that fact that catalyst **P0** is essentially inactive for the transformation, while seemingly similar catalyst **P4** is the best performing. We started our computational study by characterizing the conformational profile of these two and found two distinct classes of conformers, which we will hereafter refer to as *hairpin* and *folded* (**Figure 4a**). In the former, two (**P0**) or three (**P4**) hydrogen bonds enforce the β-turn, β-hairpin motif, with all four amino acids in a roughly planar arrangement. The *folded* conformations show the same set of hydrogen bonds but also feature an additional interaction between the *N*-terminus protecting group carbonyl and the Acpc (aminocyclopropane carboxylate) NH bond, imparting the structure a three-dimensional, helical character. These results are consistent with other studies where the conformational profiles of tetrameric peptide catalysts were investigated.[9i, 14] The key observation we made was that while **P0** shows a marked preference for the *hairpin* conformation ($\Delta G°_{hairpin\text{-}folded}$ = -2.0 kcal/mol), as it has been shown for peptides with the same backbone[9i],

https://doi.org/10.26434/chemrxiv-2023-fjfth **ORCID:** https://orcid.org/0000-0001-7817-1318

catalyst **P4** adopts a *folded* conformation ($\Delta G°_{hairpin\text{-}folded}$ = +1.2 kcal/mol). Critically, *hairpin* conformations feature a short intramolecular hydrogen bond between the guanidine and difluoracetamide moieties, while *folded* conformation do not. Therefore, we believe that catalyst **P0** is locked in an inactive state to the extent that it favors a *hairpin* conformation. *Folded* conformations, on the other hand, should be better preorganized for catalysis and more active, as observed for catalyst **P4** (**Figure 4b**). This *hairpin-folded* equilibrium will feature different biases with different hydrogen bond donor groups, and we believe the range of activities we observed for catalyst congeners is affected by this conformational dynamism. Interestingly, we found that the relative stability of these two conformations between analogs of **P4** has a linear dependence on the τ angle at the i+2 residue (R^2 = 0.86, see **Figure S12**), with the preference for a *folded* transformation increasing with the τ angle. The Acpc residue of **P4** is the strongest inducer of *folded* conformations among other i+2 residues tested, as well as the most enantioselective catalyst. Accordingly, the τ angle at the i+2 position modulates the distribution of *hairpin* and *folded* conformations, and this indirectly influences the activity and selectivity of these catalysts.

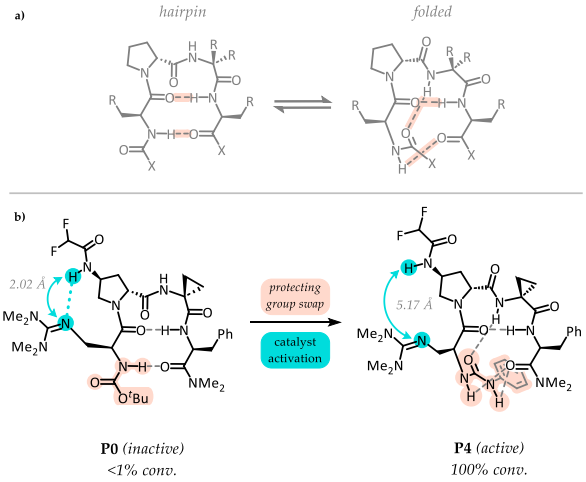

Figure 4. a: general representation of the *hairpin* and *folded* conformations families found for catalysts **P0** and **P4**. **b**: Replacing the protecting group on peptide *N*-terminus from Boc (**P0**) to *N*-phenyl carbamoyl (**P4**) activates it for catalysis: a change in the conformational preference from *hairpin* to *folded* separates the polar functionality. Catalytic reactions conversion data refers to reaction with **5a**, peptide catalyst (10 mol%), 13X MS, $PhCF_3$ (0.1 M), rt, 15 h.

Introduction of the substrate and reaction modeling. Next, the imidation reaction coordinate was modeled. Ordinarily, computational studies of peptide-based catalysts require some degree of conformational simplification due to the high number of rotatable bonds.[14-15] However, we believe that these simplifications must be adopted carefully. In the literature, we identified reports were the modeling of β–turn peptide-based catalysts only encompassed type-II β-hairpin conformation throughout the reaction coordinate.[9c, 9g, 9i] However, we found no example of computations addressing a flexible, multifunctional peptide-based catalyst that included a pendant (i.e., non-backbone amide) strong hydrogen bond donor as difluoroacetamide. This feature led us to speculate on the role of such a group in the mode of activation of the substrate and on its potential ability to (transiently) perturb the catalyst preorganization away from β-hairpin conformations. Initially, no constraints were imposed on the catalyst conformation during metadynamic conformational searches to remain open to the possibility of a substrate-induced unfolding of the catalyst. Two transition states were modeled – the first corresponding to the deprotonated amide attacking the carbamate carbonyl (TS1, *addition*), and the second corresponding to the tetrahedral intermediate releasing ethanol (TS2, *elimination*). Transition states were assembled following a bifunctional catalysis paradigm: namely, the guanidine moiety of the catalyst acting as a Brønsted base in TS1 and as a Brønsted acid in TS2, while the difluoroacetyl moiety acting as a general Brønsted acid in both transition states. Initial computations were not able to locate unfolded catalyst conformations in kinetically accessible transition states (i.e., within 10 kcal/mol at the GFN2-xTB level). Therefore, subsequent thorough investigations were carried out with the catalyst restricted to the two observed families of conformations of *folded* and *hairpin*, in order to reduce the high computational cost. The orientation of side-chain rotatable bonds of the catalyst was still thoroughly explored, with particular attention paid to the difluoroacetamide $HC(F_2)CO$ dihedral angle. Similarly to other reports on the modeling of superbasic, bifunctional organocatalysts,[16] different arrangements of catalyst and substrate moieties were explored for a total of ten different activation modes across four substrate diastereomers and two catalyst foldamer families, for a total of around 400 transition states explored (see **Figures S8** and **S9**).

TS1 - addition. In the addition step, only two out of the four possible diastereomeric intermediates are formed: these have S_a, S (hereafter S_a *anti*) and R_a, S (hereafter R_a *syn*) configurations, and only differ in the axial configuration around the C–N bond (**Figure 5b**, top row). We assessed the possibility of interconversion between these axial epimers by rotation around the hindered bond, but our modeling excluded it (lowest $\Delta\Delta G^{\ddagger}_{axis,\ intermediate}$ = 50.6 kcal/mol, lowest $\Delta\Delta G^{\ddagger}_{axis,\ product}$ = 35.6 kcal/mol). Intriguingly, the two intermediates are formed via different activation modes, coordinating with opposite hydrogen bonding acceptors on the substrate (**Figure 5b**, top row). This might arise from the energy difference between the two diastereomers: in this first endergonic step, the more stable *anti* diastereomer (TS1 S_a) benefits from more charge matching in the ground state, where the cationic guanidinium is interacting with the negatively charged amide anion. On the other hand, the least stable *syn* diastereomer (TS1 R_a) benefits from more charge matching in the product-like transition state, where the positively charged guanidinium interacts with the incipient charge on the carbamate. The energy difference between the isolated intermediates is 1.5 kcal/mol in favor of the *anti* (**Figure 5a**, *Intermediate*).

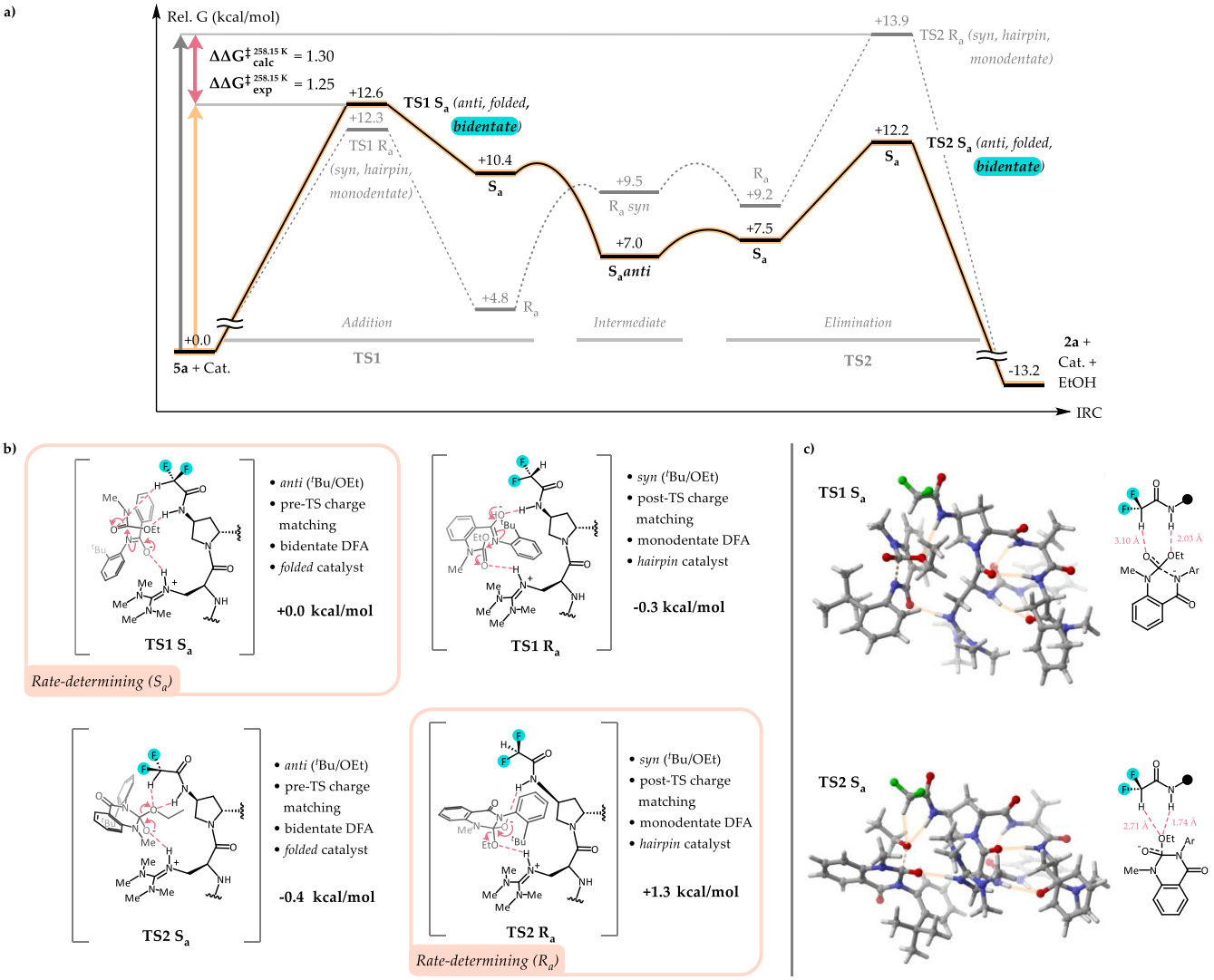

Figure 5. a: Minimum energy path for the formation of each enantiomer of **2a**. Energetic data were computed at the M06-2X/def2-QZVP/CPCM(PhCF$_3$)//R^{2}SCAN-3c/CPCM(PhCF$_3$) level. From left to right: isolated starting material **5a** and catalyst **P4**, addition transition state (**TS1**), TS1 post-reaction complex, isolated intermediates + catalyst, TS2 pre-reaction complex, elimination transition state (**TS2**), isolated product **2a** + catalyst **P4** + ethanol. **b:** Lowest energy TS geometries. The "*anti*" and "*syn*" descriptors are assigned based on the relative arrangement of the ethoxy and tert-butyl substituents on the intermediate. The "Ra" and "Sa" descriptors refer to the absolute configuration of the C–N chiral axis. Activation modes represented: top left, "TS1 Sa *anti* ethoxy *folded*"; top right, TS1 Ra *syn* flip (*hairpin*); bottom left, TS2 Sa *anti flip* (*folded*); bottom right, TS2 Ra *syn* (*hairpin*). Energetic data (free energies) are only shown for rate-determining transition states and are relative to TS1 Sa. See **Figures S8** and **S9** for a graphical representation of all the activation modes explored. Three-dimensional figures generated with CYLview 2.0.[17] DFA: difluoroacetamide moiety. **c**: Hydrogen bond distances for the difluoroacetamide moiety on TS1 Sa and TS2 Sa, both featuring bidentate coordination.

TS2 - elimination. The two diastereomeric intermediates are formed at roughly identical rates ($\Delta\Delta G^{\ddagger}_{TS1\ Ra/Sa}$ = 0.3 kcal/mol), but while the Ra *syn* isomer is formed reversibly, the formation of the Sa *anti* isomer is irreversible, and it is promptly transformed into the major product via TS2 Sa (**Figure 5a**, TS2). Therefore, *each enantiomer of the product emerges from a mechanistically different rate-determining step*, and the energy difference between these accounts for the observed selectivity (TS1 Sa and TS2 Ra, **Figure 5**). The predicted $\Delta\Delta G^{\ddagger}_{calc}$ is 1.30 kcal/mol (corresponding to 7:93 er at -15 °C), which is in optimal agreement with the experimentally observed value of 1.25 kcal/mol (8:92 er at -15 °C).

Rate-decrease of brominated substrate. The experimental observation that brominated substrate **5c** reacted orders of magnitude slower than lead substrate **5a** (**Figure 3**) prompted us to find a computationally corroborated rationale for this phenomenon. Direct replacement of the designated C–H bond with a C–Br bond in the two rate-determining transition states for **5a** and re-optimization furnished two transition states for **5c**. In line with experimental observations, the activation energies for **5c** are significatively higher than **5a** (18.8 and 19.8 kcal/mol for **5c**, 12.6 and 13.9 kcal/mol for **5a**). Interestingly, both transition states go up in energy even if there is no apparent clash being introduced by the bromine atom in any of the two. Moreover, the two elementary steps are expected to display opposite electronic trends, yet both barriers increase with the introduction of an electronegative atom. In fact, the origin of the rate decrease was not identified in a steric or an electronic argument, but in an entropic one: a larger

negative value of $\Delta S^{\ddagger}$ for brominated substrate **5c** relative to the unsubstituted substrate **5a**. The vibrational freedom of the **5c** starting material is significatively larger than **5a**, causing the former to suffer a much greater entropic penalty in the transition states. This results in an increase of both the TS1 R_a and TS2 S_a reaction barriers. (See **Table S6**).

Difluoroacetamide – mono- vs. bidentate coordination. Having access to the detailed intermolecular interactions responsible for selectivity, we identified the unique role of the difluoroacetamide moiety as a versatile mono- *and* bidentate hydrogen bond donor. The HCCO angle of the difluoroacetamide (DFA) moiety is a paramount feature in defining the energetic profile of the transition states, as suboptimal orientations perturb the (electronic) energy up to ~2 kcal/mol. The best orientation of this group is governed by two opposing factors: while the intrinsic conformational preference of the DFA group is *gauche*, the *syn* conformation is a better hydrogen bond donor (**Figure 6**).[18] While in the pro-R_a transition states its preferential orientation is minimizing the local and possibly the overall dipole (TS1 R_a, TS2 R_a, α_{HCCO} ~ +50°/-50°, *gauche*) in the pro-S_a transition states it acts as an asymmetric bidentate hydrogen bond donor, at the cost of *maximizing* the local and overall dipole (TS1 S_a, TS2 S_a, α_{HCCO} ~ +165°, *syn,* **Figure 5c** and **6**). The profile of this non-covalent interaction was assessed via comparison of the CH-O distances and via the qualitative presence of interaction surfaces as visualized by NCIPLOT[19] (**Figure S11**).

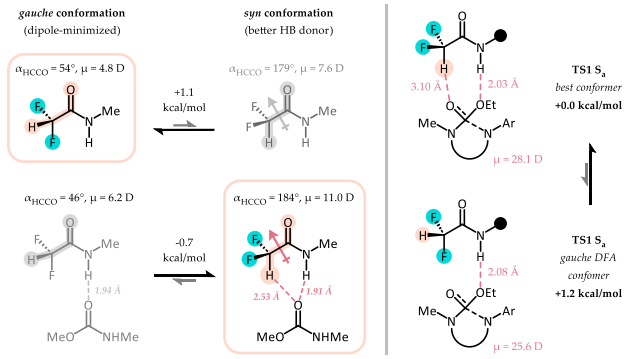

Figure 6. Right side: the difluoroacetamide *syn* conformer is a better hydrogen bond donor than the *gauche* towards a simple carbamate Lewis base. Energy values given are based on interaction free energies. Dipole moments were extracted from higher-level single point calculations. Left side: suboptimal orientation of the difluoroacetamide moiety in TS1 S_a penalize the energy more than 1 kcal/mol. All energetic and spatial data were computed at the M06-2X/def2-QZVP/CPCM($PhCF_3$)//R²SCAN-3c/CPCM($PhCF_3$) level.

We believe that this differential ability to act as an asymmetric, double hydrogen bond donor (HBD) *exclusively* for pro-S_a transition states is a key factor in determining the reaction selectivity. Both monodentate (acetamido, methoxycarbonylamido) and bidentate (phenylureido) HBDs showed significantly reduced levels of selectivity. Our modeling suggests that the DFA group, in the context of the reaction, has a nuanced ability to differentiate activation modes by differentially acting as a mono- *or* bidentate HBD (**Figure 7**). While stronger, strictly bidentate HBDs show a greater tendency to interact as bidentate under *all* activation modes (thus not differentiating them), asymmetric NH/CH bidentate HBDs can have an enhanced ability to discriminate between mono- and bidentate. Most likely, in the case of DFA, this is also due to meaningful contributions on the overall dipole from the different *syn*/*gauche* conformations. Breaking the quasi-degeneracy of activation modes is beneficial in cases where different arrangements lead to the formation of different stereoisomers. Our computational modeling reflects such a scenario: for example, the activation mode "TS1 ethoxy" favors the R_a syn intermediate, and switching hydrogen bonding partners gives the activation mode "TS1 flip", which favors the S_a anti product. Mode "TS2" favors the R_a product while mode "TS2 flip" favors the S_a product (see **Figures S8** and **S9** for a graphical representation of all the activation modes). Effectively, all four productive transition states (**Figures 5**) feature topologically different activation modes. Therefore, we believe activation mode discrimination directly induces enantiodiscrimination.

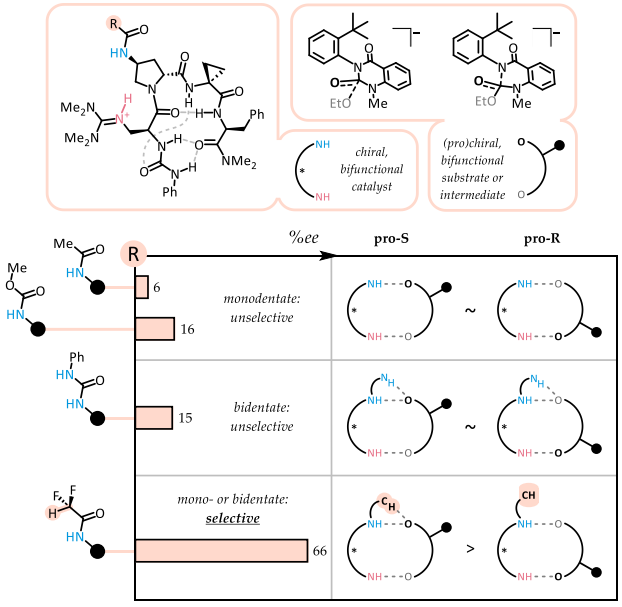

Figure 7. Activation mode degeneracy breaking as a strategy for enantiodiscrimination. Enantiomeric excess (ee) data obtained for reaction with substrate **5a** and depicted catalysts (10% mol) - 5 Å MS (400 mg/mmol **5a**), $PhCF_3$ 0.1 M, 15 h, rt.

Conclusions. In conclusion, we developed a new class of superbasic, bifunctional peptidyl guanidine catalysts to address a specific stereogenic element within a recently disclosed bioactive scaffold, namely an *N*-aryl quinazolinedione. The underlying basis of the atroposelectivity delivered by the structurally novel catalyst was rationalized through a systematic computational analysis of successful and unsuccessful catalyst designs, as well as of the dissection of their influence on the asymmetric reaction. Nominally, the requirement of a *N*'-phenyl carbamoyl *N*-terminus end cap was traced back to its conformational biasing of the catalyst *hairpin-folded* conformational equilibrium towards the *folded* form, a preference opposite to the more common Boc group. This conformational change helps to separate the guanidine and difluoroacetamide

moieties, effecting a "switch-on" of catalytic activity. Our modeling unveiled high levels of preorganization within this novel scaffold, which proved amenable to backbone functionalization with strong hydrogen bond donors (HBD) without perturbing catalyst folding. The unusual difluoroacetamide (DFA) group, installed on the 4-position of a critical proline residue, proved uniquely selective against other mono- and bidentate HBDs of various strengths. This effect was traced back to its ability to act either as a monodentate *or* as a bidentate HBD across two reaction steps, where only the favored enantiomer transition states feature bidentate coordination. Computational studies of this breadth and conformational complexity (~400 transition states) are very scarce in asymmetric catalysis, and to the best of our knowledge have no precedent in the context of small peptide asymmetric catalysis. We anticipate this work will constitute a successful precedent for the modeling and understanding of conformationally flexible systems and large reaction spaces that constitute a challenge to the design of complex asymmetric reactions. We are currently leveraging the conformational insights obtained from this work developing new catalysts to unlock novel selective reactions.

ASSOCIATED CONTENT

Supporting Information. The Supporting Information is available free of charge at [...].

Accession codes. CCDC 2300978, 2300979, 2300980, and 2300981 contain the supplementary crystallographic data for this paper. These data can be obtained free of charge via www.ccdc.cam.ac.uk/data_request/cif, or by emailing data_request@ccdc.cam.ac.uk, or by contacting The Cambridge Crystallographic Data Centre, 12 Union Road, Cambridge CB2 1EZ, U.K.; fax: +44 1223 336033.

AUTHOR INFORMATION

Corresponding Author

Scott J. Miller – Department of Chemistry, Yale University, New Haven, Connecticut 06520-8107, United States; orcid.org/0000-0001-7817-1318; Email: scott.miller@yale.edu

Authors

Nicolò Tampellini – Department of Chemistry, Yale University, New Haven, Connecticut 06520-8107, United States; orcid.org/0000-0002-6611-556X; Email: nicolo.tampellini@yale.edu

Brandon Q. Mercado – Department of Chemistry, Yale University, New Haven, Connecticut 06520-8107, United States; orcid.org/0000-0002-1940-3497; Email: brandon.mercado@yale.edu

Notes

The authors declare no competing financial interest.

Acknowledgements

The authors would like to thank Jenny Tan for helping with the synthesis of some of the substrates and catalysts. Dr. Omar Beleh and Dr. Jonathan Ryss are thanked for initial exploration of guanidyl peptides reactivity. Dr. Fabian Menges is thanked for HRMS analysis. This work was supported by the National Institute of General Medical Sciences of the U.S. National Institutes of Health (R35 GM132092 to S.J.M.). The authors are thankful to the Yale Center for Research Computing (YCRC) for the resources provided.

References

1. (a) Watterson, S. H.; De Lucca, G. V.; Shi, Q.; Langevine, C. M.; Liu, Q.; Batt, D. G.; Beaudoin Bertrand, M.; Gong, H.; Dai, J.; Yip, S.; Li, P.; Sun, D.; Wu, D.-R.; Wang, C.; Zhang, Y.; Traeger, S. C.; Pattoli, M. A.; Skala, S.; Cheng, L.; Obermeier, M. T.; Vickery, R.; Discenza, L. N.; D'Arienzo, C. J.; Zhang, Y.; Heimrich, E.; Gillooly, K. M.; Taylor, T. L.; Pulicicchio, C.; McIntyre, K. W.; Galella, M. A.; Tebben, A. J.; Muckelbauer, J. K.; Chang, C.; Rampulla, R.; Mathur, A.; Salter-Cid, L.; Barrish, J. C.; Carter, P. H.; Fura, A.; Burke, J. R.; Tino, J. A. Discovery of 6-Fluoro-5-(R)-(3-(S)-(8-fluoro-1-methyl-2,4-dioxo-1,2-dihydroquinazolin-3(4H)-yl)-2-methylphenyl)-2-(S)-(2-hydroxypropan-2-yl)-2,3,4,9-tetrahydro-1H-carbazole-8-carboxamide (BMS-986142): A Reversible Inhibitor of Bruton's Tyrosine Kinase (BTK) Conformationally Constrained by Two Locked Atropisomers. *J. Med. Chem.* **2016,** *59* (19), 9173-9200; (b) Gonzalez, F. L.; Wisniewski, S. R.; Katipally, K.; Stevens, J. M.; Rosso, V.; Mack, B.; Razler, T. M. Systematic Optimization of a Robust Telescoped Process for a BTK Inhibitor with Atropisomer Control by High-Throughput Experimentation, Design of Experiments, and Linear Regression. *Org. Process. Res. Dev.* **2019,** *23* (6), 1143-1151.
2. Dhillon, S. Carotegrast Methyl: First Approval. *Drugs* **2022,** *82* (9), 1011-1016.
3. Siller-Matula, J. M.; Krumphuber, J.; Jilma, B. Pharmacokinetic, pharmacodynamic and clinical profile of novel antiplatelet drugs targeting vascular diseases. *Br. J. Pharmacol.* **2010,** *159* (3), 502-517.
4. (a) Cheng, J. K.; Xiang, S.-H.; Li, S.; Ye, L.; Tan, B. Recent Advances in Catalytic Asymmetric Construction of Atropisomers. *Chem. Rev.* **2021,** *121* (8), 4805-4902; (b) Rodríguez-Salamanca, P.; Fernández, R.; Hornillos, V.; Lassaletta, J. M. Asymmetric Synthesis of Axially Chiral C–N Atropisomers. *Chem. Eur. J.* **2022,** *28* (28), e202104442.
5. Zou, Y.; Yang, S.; Sanders, J. N.; Li, W.; Yu, P.; Wang, H.; Tang, Z.; Liu, W.; Houk, K. N. Computational Investigation of the Mechanism of Diels-Alderase PyrI4. *J. Am. Chem. Soc.* **2020,** *142* (47), 20232-20239.
6. (a) Krawczyk, H.; Dzięgielewski, M.; Deredas, D.; Albrecht, A.; Albrecht, Ł. Chiral Iminophosphoranes—An Emerging Class of Superbase Organocatalysts. *Chem. Eur. J.* **2015,** *21* (29), 10268-10277; (b) Teng, B.; Lim, W. C.; Tan, C.-H. Recent Advances in Enantioselective Brønsted Base Organocatalytic Reactions. *Synlett* **2017,** *28* (11), 1272-1277; (c) Chou, H.-C.; Leow, D.; Tan, C.-H. Recent Advances in Chiral Guanidine-Catalyzed Enantioselective Reactions. *Chemistry – An Asian Journal* **2019,** *14* (21), 3803-3822; (d) Formica, M.; Rozsar, D.; Su, G.; Farley, A. J. M.; Dixon, D. J. Bifunctional Iminophosphorane Superbase Catalysis: Applications in Organic Synthesis. *Acc. Chem. Res.* **2020,** *53* (10), 2235-2247; (e) Vazdar, K.; Margetić, D.; Kovačević, B.; Sundermeyer, J.; Leito, I.; Jahn, U. Design of Novel Uncharged Organic Superbases: Merging Basicity and Functionality. *Acc. Chem. Res.* **2021,** *54* (15), 3108-3123.
7. Beleh, O. M.; Miller, E.; Toste, F. D.; Miller, S. J. Catalytic Dynamic Kinetic Resolutions in Tandem to Construct Two-Axis Terphenyl Atropisomers. *J. Am. Chem. Soc.* **2020,** *142* (38), 16461-16470.
8. (a) Jarvo, E. R.; Copeland, G. T.; Papaioannou, N.; Bonitatebus, P. J.; Miller, S. J. A Biomimetic Approach to Asymmetric Acyl Transfer Catalysis. *J. Am. Chem. Soc.* **1999,** *121* (50), 11638-11643; (b) Crawford, J. M.; Sigman, M. S. Conformational Dynamics in Asymmetric Catalysis: Is Catalyst Flexibility a Design Element? *Synthesis* **2019,** *51* (05), 1021-1036; (c) Girvin, Z. C.; Gellman, S. H. Foldamer Catalysis. *J. Am. Chem. Soc.* **2020,** *142* (41), 17211-17223; (d) Metrano, A. J.; Chinn, A. J.; Shugrue, C. R.; Stone, E. A.; Kim, B.; Miller, S. J. Asymmetric Catalysis Mediated by Synthetic Peptides, Version 2.0: Expansion of Scope and Mechanisms. *Chem. Rev.* **2020,** *120* (20), 11479-11615.
9. (a) Doyle, A. G.; Jacobsen, E. N. Small-Molecule H-Bond Donors in Asymmetric Catalysis. *Chem. Rev.* **2007,** *107* (12), 5713-5743; (b) Parmar, D.; Sugiono, E.; Raja, S.; Rueping, M. Complete Field Guide to Asymmetric BINOL-Phosphate Derived Brønsted Acid and Metal Catalysis: History and Classification by Mode of Activation; Brønsted Acidity, Hydrogen Bonding, Ion Pairing, and Metal Phosphates. *Chem. Rev.* **2014,** *114* (18), 9047-9153; (c) Liao, R.-Z.; Santoro, S.; Gotsev, M.; Marcelli, T.; Himo, F. Origins of

Stereoselectivity in Peptide-Catalyzed Kinetic Resolution of Alcohols. *ACS Catalysis* **2016,** *6* (2), 1165-1171; (d) Wheeler, S. E.; Seguin, T. J.; Guan, Y.; Doney, A. C. Noncovalent Interactions in Organocatalysis and the Prospect of Computational Catalyst Design. *Acc. Chem. Res.* **2016,** *49* (5), 1061-1069; (e) Davis, H. J.; Phipps, R. J. Harnessing non-covalent interactions to exert control over regioselectivity and site-selectivity in catalytic reactions. *Chemical Science* **2017,** *8* (2), 864-877; (f) Toste, F. D.; Sigman, M. S.; Miller, S. J. Pursuit of Noncovalent Interactions for Strategic Site-Selective Catalysis. *Acc. Chem. Res.* **2017,** *50* (3), 609-615; (g) Shi, Q.; Xu, M.; Chang, R.; Ramanathan, D.; Peñin, B.; Funes-Ardoiz, I.; Ye, J. Visible-light mediated catalytic asymmetric radical deuteration at non-benzylic positions. *Nature Communications* **2022,** *13* (1), 4453; (h) Vastakaite, G.; Grünenfelder, C. E.; Wennemers, H. Peptide-Catalyzed Stereoselective Conjugate Addition Reaction of Aldehydes to C-Substituted Maleimides. *Chem. Eur. J.* **2022,** *28* (18), e202200215; (i) Hejna, B. G.; Ganley, J. M.; Shao, H.; Tian, H.; Ellefsen, J. D.; Fastuca, N. J.; Houk, K. N.; Miller, S. J.; Knowles, R. R. Catalytic Asymmetric Hydrogen Atom Transfer: Enantioselective Hydroamination of Alkenes. *J. Am. Chem. Soc.* **2023,** *145* (29), 16118-16129.

10. (a) Diener, M. E.; Metrano, A. J.; Kusano, S.; Miller, S. J. Enantioselective Synthesis of 3-Arylquinazolin-4(3H)-ones via Peptide-Catalyzed Atroposelective Bromination. *J. Am. Chem. Soc.* **2015,** *137* (38), 12369-12377; (b) Kennedy, C. R.; Lehnherr, D.; Rajapaksa, N. S.; Ford, D. D.; Park, Y.; Jacobsen, E. N. Mechanism-Guided Development of a Highly Active Bis-thiourea Catalyst for Anion-Abstraction Catalysis. *J. Am. Chem. Soc.* **2016,** *138* (41), 13525-13528; (c) Procházková, E.; Kolmer, A.; Ilgen, J.; Schwab, M.; Kaltschnee, L.; Fredersdorf, M.; Schmidts, V.; Wende, R. C.; Schreiner, P. R.; Thiele, C. M. Uncovering Key Structural Features of an Enantioselective Peptide-Catalyzed Acylation Utilizing Advanced NMR Techniques. *Angew. Chem. Int. Ed.* **2016,** *55* (51), 15754-15759; (d) Rigling, C.; Kisunzu, J. K.; Duschmalé, J.; Häussinger, D.; Wiesner, M.; Ebert, M.-O.; Wennemers, H. Conformational Properties of a Peptidic Catalyst: Insights from NMR Spectroscopic Studies. *J. Am. Chem. Soc.* **2018,** *140* (34), 10829-10838; (e) Schreyer, L.; Properzi, R.; List, B. IDPi Catalysis. *Angew. Chem. Int. Ed.* **2019,** *58* (37), 12761-12777; (f) Genov, G. R.; Douthwaite, J. L.; Lahdenperä, A. S. K.; Gibson, D. C.; Phipps, R. J. Enantioselective remote C–H activation directed by a chiral cation. *Science* **2020,** *367* (6483), 1246-1251.

11. Bandar, J. S.; Lambert, T. H. Enantioselective Brønsted Base Catalysis with Chiral Cyclopropenimines. *J. Am. Chem. Soc.* **2012,** *134* (12), 5552-5555.

12. Núñez, M. G.; Farley, A. J. M.; Dixon, D. J. Bifunctional Iminophosphorane Organocatalysts for Enantioselective Synthesis: Application to the Ketimine Nitro-Mannich Reaction. *J. Am. Chem. Soc.* **2013,** *135* (44), 16348-16351.

13. (a) Harvey, J. N.; Himo, F.; Maseras, F.; Perrin, L. Scope and Challenge of Computational Methods for Studying Mechanism and Reactivity in Homogeneous Catalysis. *ACS Catalysis* **2019,** *9* (8), 6803-6813; (b) Gorbachev, V.; Tsybizova, A.; Miloglyadova, L.; Chen, P. Increasing Complexity in a Conformer Space Step-by-Step: Weighing London Dispersion against Cation−π Interactions. *J. Am. Chem. Soc.* **2022,** *144* (20), 9007-9022; (c) Stone, E. A.; Hosseinzadeh, P.; Craven, T. W.; Robertson, M. J.; Han, Y.; Hsieh, S.-Y.; Metrano, A. J.; Baker, D.; Miller, S. J. Isolating Conformers to Assess Dynamics of Peptidic Catalysts Using Computationally Designed Macrocyclic Peptides. *ACS Catalysis* **2021,** *11* (8), 4395-4400.

14. Metrano, A. J.; Abascal, N. C.; Mercado, B. Q.; Paulson, E. K.; Hurtley, A. E.; Miller, S. J. Diversity of Secondary Structure in Catalytic Peptides with β-Turn-Biased Sequences. *J. Am. Chem. Soc.* **2017,** *139* (1), 492-516.

15. Mishra, P.; Hewett, D. M.; Zwier, T. S. Conformational explosion: Understanding the complexity of short chain para-dialkylbenzene potential energy surfaces. *The Journal of Chemical Physics* **2018,** *148* (18), 184304.

16. Su, G.; Formica, M.; Yamazaki, K.; Hamlin, T. A.; Dixon, D. J. Catalytic Enantioselective Intramolecular Oxa-Michael Reaction to α,β-Unsaturated Esters and Amides. *J. Am. Chem. Soc.* **2023,** *145* (23), 12771-12782.

17. Legault, P. C. Y. *CYLview*, 2020.

18. (a) Koeller, S.; Thomas, C.; Peruch, F.; Deffieux, A.; Massip, S.; Léger, J.-M.; Desvergne, J.-P.; Milet, A.; Bibal, B. α-Halogenoacetanilides as Hydrogen-Bonding Organocatalysts that Activate Carbonyl Bonds: Fluorine versus Chlorine and Bromine. *Chem. Eur. J.* **2014,** *20* (10), 2849-2859; (b) Cosimi, E.; Trapp, N.; Ebert, M.-O.; Wennemers, H. Combined experimental and theoretical study of long-range H–F interactions in α-fluoro amides. *Chem. Commun.* **2019,** *55* (16), 2253-2256.

19. Contreras-García, J.; Johnson, E. R.; Keinan, S.; Chaudret, R.; Piquemal, J.-P.; Beratan, D. N.; Yang, W. NCIPLOT: A Program for Plotting Noncovalent Interaction Regions. *J. Chem. Theory Comput.* **2011,** *7* (3), 625-632.